Astronomy & Astrophysics

Pulsar-wind-nebula-powered Galactic center X-ray filament G0.13–0.11

Proof of the synchrotron nature by IXPE

Eugene Churazov[1,2], Ildar Khabibullin[3,1,2], Thibault Barnouin[4], Niccolò Bucciantini[5,6,7], Enrico Costa[8], Laura Di Gesu[9], Alessandro Di Marco[8], Riccardo Ferrazzoli[8], William Forman[10], Philip Kaaret[11], Dawoon E. Kim[8,12,53], Jeffery J. Kolodziejczak[11], Ralph Kraft[10], Frédéric Marin[4], Giorgio Matt[14], Michela Negro[15], Roger W. Romani[16], Stefano Silvestri[17,24], Paolo Soffitta[8], Rashid Sunyaev[1,2], Jiri Svoboda[18], Alexey Vikhlinin[10], Martin C. Weisskopf[11], Fei Xie[19,8], Iván Agudo[20], Lucio A. Antonelli[21,22], Matteo Bachetti[23], Luca Baldini[17,24], Wayne H. Baumgartner[11], Ronaldo Bellazzini[17], Stefano Bianchi[14], Stephen D. Bongiorno[11], Raffaella Bonino[25,26], Alessandro Brez[17], Fiamma Capitanio[8], Simone Castellano[17], Elisabetta Cavazzuti[9], Chien-Ting Chen[27], Stefano Ciprini[13,22], Alessandra De Rosa[8], Ettore Del Monte[8], Niccolò Di Lalla[16], Immacolata Donnarumma[9], Victor Doroshenko[28], Michal Dovčiak[18], Steven R. Ehlert[11], Teruaki Enoto[29], Yuri Evangelista[8], Sergio Fabiani[8], Javier A. García[30], Shuichi Gunji[31], Kiyoshi Hayashida[32], Jeremy Heyl[33], Wataru Iwakiri[34], Svetlana G. Jorstad[35,36], Vladimir Karas[18], Fabian Kislat[37], Takao Kitaguchi[29], Henric Krawczynski[38], Fabio La Monaca[8,49,12], Luca Latronico[25], Ioannis Liodakis[11], Simone Maldera[25], Alberto Manfreda[39], Andrea Marinucci[9], Alan P. Marscher[35], Herman L. Marshall[40], Francesco Massaro[25,26], Ikuyuki Mitsuishi[41], Tsunefumi Mizuno[42], Fabio Muleri[8], Chi-Yung Ng[43], Stephen L. O'Dell[11], Nicola Omodei[16], Chiara Oppedisano[25], Alessandro Papitto[21], George G. Pavlov[44], Abel L. Peirson[16], Matteo Perri[22,21], Melissa Pesce-Rollins[17], Pierre-Olivier Petrucci[45], Maura Pilia[23], Andrea Possenti[23], Juri Poutanen[46], Simonetta Puccetti[22], Brian D. Ramsey[11], John Rankin[8], Ajay Ratheesh[8], Oliver J. Roberts[27], Carmelo Sgrò[17], Patrick Slane[10], Gloria Spandre[17], Douglas A. Swartz[27], Toru Tamagawa[29], Fabrizio Tavecchio[47], Roberto Taverna[48], Yuzuru Tawara[41], Allyn F. Tennant[11], Nicholas E. Thomas[11], Francesco Tombesi[49,13,50], Alessio Trois[23], Sergey S. Tsygankov[46], Roberto Turolla[48,51], Jacco Vink[52], Kinwah Wu[51], and Silvia Zane[51]

(Affiliations can be found after the references)

ABSTRACT

We report the discovery of X-ray polarization from the X-ray-bright filament G0.13−0.11 in the Galactic center (GC) region. This filament features a bright, hard X-ray source that is most plausibly a pulsar wind nebula (PWN) and an extended and structured diffuse component. Combining the polarization signal from IXPE with the imaging/spectroscopic data from *Chandra*, we find that X-ray emission of G0.13−0.11 is highly polarized PD = 57(±18)% in the 3−6 keV band, while the polarization angle is PA = 21°(±9°). This high degree of polarization proves the synchrotron origin of the X-ray emission from G0.13−0.11. In turn, the measured polarization angle implies that the X-ray emission is polarized approximately perpendicular to a sequence of nonthermal radio filaments that may be part of the GC Radio Arc. The magnetic field on the order of $100 \, \mu$G appears to be preferentially ordered along the filaments. The above field strength is the fiducial value that makes our model self-consistent, while the other conclusions are largely model independent.

Key words. magnetic fields – polarization – radiation mechanisms: non-thermal – scattering – X-rays: general

1. Introduction

The origin of spectacular radio filaments (including the most prominent Radio Arc) in the Galactic center (GC) region and the role of pulsar wind nebulae (PWNe) in their appearance is an actively debated topic (e.g., Yusef-Zadeh et al. 2004). Many of the observed radio filaments have spectral and polarization properties suggesting that they are dominated by non-thermal emission (e.g Yusef-Zadeh et al. 1984; Tsuboi et al. 1986; Lang et al. 1999; LaRosa et al. 2004; Heywood et al. 2019). Hereafter, we refer to them as nonthermal filaments (NTFs).

Some of the NTFs have known X-ray counterparts. Here, we focus on one of them – an X-ray/radio thread G0.13−0.11. In the X-ray band, G0.13−0.11 was studied by Yusef-Zadeh et al. (2002), Wang et al. (2002), and Zhang et al. (2020) using *Chandra* and *NuSTAR* data. The case of G0.13−0.11 is especially interesting due to the close correspondence of X-ray structures and a subsystem of the Radio Arc filaments noted by Yusef-Zadeh et al. (2002), Wang et al. (2002). Based on a filamentary X-ray appearance, the presence of a compact source, and a nonthermal spectrum, the latter two studies focused on the interpretation of G0.13−0.11 as a PWN with a filament formed

by leptons escaping from the supersonically moving PWN into the ambient magnetic field (see, e.g., Gaensler & Slane 2006; Kargaltsev et al. 2017; Bykov et al. 2017; Olmi & Bucciantini 2023, for reviews).

In the standard PWN scenario, described in the aforementioned reviews, a pulsar generates an ultrarelativistic electron-positron wind that passes through its termination shock and gives rise to a wind nebula filled with high-energy leptons. For a supersonically moving PWN, a bow shock is formed ahead of the source. In this class of models, known as bow-shock PWN (BSPWN), the leptons with a sufficiently large Lorentz factor (and, hence, a large gyroradius) can cross the bow-shock region and escape the source (Bandiera 2008). Bykov et al. (2017, see their Sect. 6) discussed conditions needed to produce very hard spectra (dominated by the highest energies) and a reconnection scenario that can lead to asymmetric or one-sided X-ray structures observed in several BSPWNs, such as the Lighthouse (Pavan et al. 2011) or Guitar (de Vries et al. 2022) nebulae. In this scenario, the mutual orientation of the PWN and the ambient magnetic fields set the topology of the field lines in a way reminiscent of Earth's magnetosphere embedded in the solar wind. Numerical magneto-hydrodynamical (MHD) models of these objects appear to be in reasonable agreement with observations (e.g., Barkov et al. 2019; Olmi & Bucciantini 2019). In these models, the radio and X-ray fluxes from threads are produced by synchrotron emission of relativistic leptons and hence should be polarized, if the magnetic field is at least partly ordered. Now, IXPE (Weisskopf et al. 2022) can test this prediction in the X-ray regime. In the X-ray regime, the polarization angle (PA) is expected to be perpendicular to the orientation of the magnetic field, and, unlike the radio data (e.g., Paré et al. 2019, 2021), it is not affected by the Faraday rotation and depolarization due to foreground magnetized plasma.

Should IXPE observations place tight upper limits on the polarization degree, this would imply either that the diffuse X-ray emission is not due to the synchrotron mechanism or that the magnetic field is highly disordered. The former assumption would contradict the basic model of PWN-powered X-ray extended structures and create a major problem not only for G0.13−0.11 but for the entire class of these objects. The latter possibility would imply that magnetic field topology in the regions contributing to the X-ray emission is very different (much more tangled) from that in the nearby radio-emitting filaments, which have highly ordered fields based on observations at 1−100 GHz frequencies (e.g., Guan et al. 2021). Yet another possibility, discussed in Yusef-Zadeh et al. (2002), is that G0.13−0.11 is not a PWN, and low-energy cosmic-ray electrons produce the power-law continuum by bremsstrahlung emission in the X-ray band.

2. Data

In this work, we used the data of two IXPE observations of the GC region, more specifically, a complex of molecular clouds ~0.1° to the east of Sgr A* (Marin et al. 2023). These observations with a total clean exposure time of 1.8 Ms, were performed in two parts – in February 2022 and September 2023. These two observations were centered on (RA, Dec) = (266.51, −28.89) and (266.57, −28.89), respectively, with an offset between them of ~3′. The data were processed with the standard IXPE pipeline. The output FITS files of this pipeline contain the event-by-event Stokes parameters (see Kislat et al. 2015) from which the polarization observables of the X-ray radiation can be derived. The data products are publicly available for use by the interna-

tional astrophysics community at the High-Energy Astrophysics Science Archive Research Center (HEASARC, at the NASA Goddard Space Flight Center). An energy-dependent particle background rejection algorithm based on photoelectron-track ellipticity was applied to these level-2 event files; it allows the removal of ~40% of the instrumental background (Di Marco et al. 2023). In addition, observation times affected by increased background due to solar activity were removed (see Marin et al. 2023 for additional details on the procedure).

High spatial resolution X-ray images were obtained with *Chandra* over multiple observing campaigns from 2000 to 2022. The total exposure of the *Chandra* pointings with G0.13−0.11 located in the central region of the field of view (FOV) with high spatial resolution is 1.4 Ms. The *Chandra* data reduction follows a standard procedure based on the latest versions of the data reduction software (CIAO v. 4.14) and calibration (CALDB v. 4.9.8). Our particular approach and analysis steps are described in detail in Vikhlinin et al. (2009). Briefly, they include the identification and removal of high background periods, the correction of photon energies for the time and detector temperature dependence of the charge transfer inefficiency and gain, and the creation of matching background datasets using blank sky observations with exposure times similar to the GC pointings. For the analysis presented here, we used the combined flat-fielded and background-subtracted *Chandra* image in the 2.3−8 keV band and spectra extracted in several elliptical regions, as described below. Following the standard approach for analyzing *Chandra* spectra of extended sources, we have generated the spectral response files that combine the position-dependent ACIS calibration with the weights proportional to the observed brightness. In the radio band, we used publicly available MeerKAT images[1] at the central frequency of 1.3 GHz and ~6″ angular resolution (see Heywood et al. 2022 for a detailed description).

Figure 1 shows a combination of the *Chandra* X-ray image in the 2.3−8 keV band (in green) and the MeerKAT radio image (in red). G0.13−0.11 is a green feature to the right of a triangular-shaped sequence of NTFs near the center of the image. The cyan lines show the polarization angle of the G0.13−0.11 X-ray emission (best-fitting value ±1σ error) measured by IXPE.

3. X-ray images and spectra

The X-ray images of the G0.13−0.11 region in the 2−8 keV band obtained by IXPE and *Chandra* are shown in Fig. 2. The images were smoothed with a Gaussian filter with $\sigma = 5''$ and 0.5″ for IXPE and *Chandra*, respectively. G0.13−0.11 is located in the bottom left corner of the image and is clearly visible as a pair of bright wings in the *Chandra* image. Sgr A* is outside of the region shown, ~0.06° from the right boundary.

With the approach outlined above, IXPE will provide the polarized emission (Q and U spectra) of the entire region, while *Chandra* data resolve the spectrum into spatially distinct components, in particular, the nonthermal component. The *Chandra* image with the additional regions used for spectra extraction is shown in Fig. 3, including a point source CXOGCS J174621.5−285256 marked with the blue circle (SRC), two narrow green boxes covering the brightest part of the box-shaped structure (Wings-n), a larger red ellipse that covers the "wings" and a more extended structure to the left of the wings (Wings-e), and the entire IXPE region (black). The latter region ($\approx 43 \times 60''$) is the same as shown in Fig. 2. In the 2022
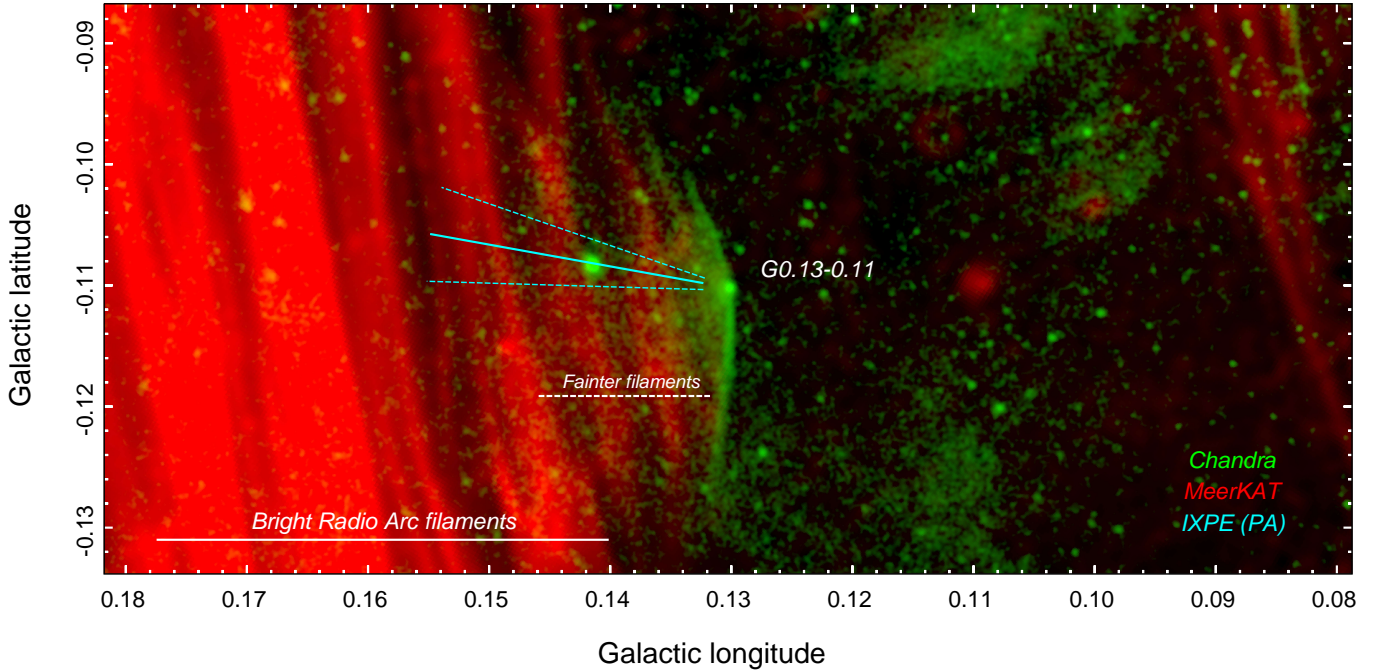
---

[1] https://doi.org/10.48479/fyst-hj47

Fig. 1. Combination of radio (MeerKAT; 1.3 GHz, red) and X-ray (*Chandra*; 2.3−8 keV, Log scale, smoothed with $\sigma = 0.5''$ Gaussian, green) images of the G0.13−0.11 region in Galactic coordinates. The cyan lines show the constraints on the polarization angle (PA) of the G0.13−0.11 emission derived from the IXPE data (best-fitting value ±1σ error; i.e., 21 ± 9°). The prominent red vertical threads on the left side of the image belong to the NTFs of the Radio Arc. G0.13−0.11 is the green feature to the east of a sequence of fainter NTFs near the center of the image. G0.13−0.11 consists of (i) a compact core (the bright green dot at the center of the figure; presumably the pulsar itself and its PWN); (ii) a pair of bright "wings"; and (iii) a more diffuse (possibly structured) X-ray glow to the left of the "wings" (at higher Galactic longitude). The polarization direction is approximately perpendicular to the X-ray "wings" and the nearest NTFs. Coupled with the large polarization degree, this proves that X-rays are produced by synchrotron emission of ~TeV electrons.
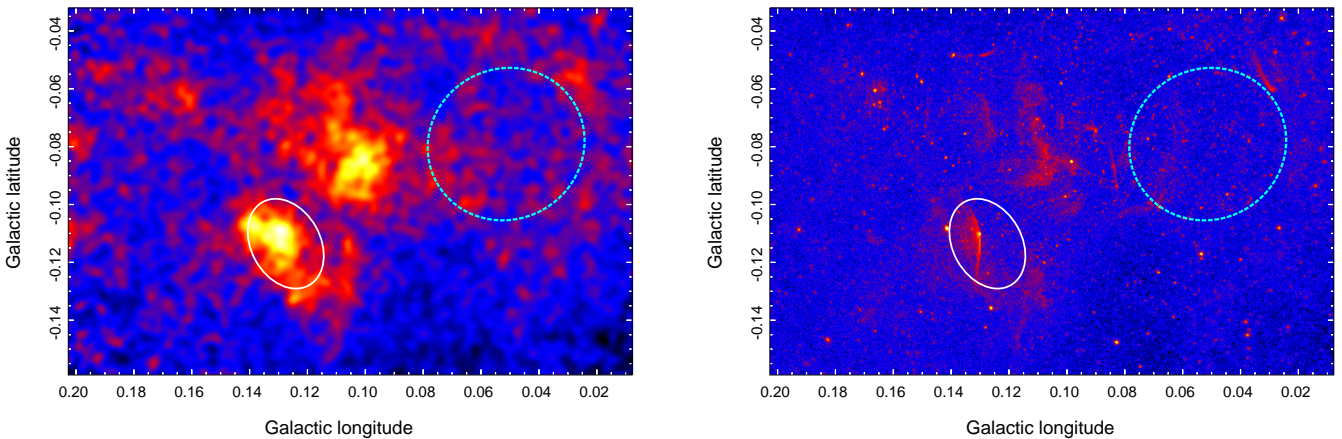

Fig. 2. 3−6 keV IXPE (left panel) and *Chandra* (right panel) X-ray images. Two elliptical regions were used for spectra extraction. The white ellipse covers the G0.13−0.11 area. Given the uncertainties with the IXPE astrometry, a relatively large region was selected guided by the IXPE image. The bigger cyan region was used as a background region for spectral analysis. The *Chandra* image is in logarithmic scale to show more clearly bright point sources and faint diffuse emission. For the IXPE image, a linear scale is used.

and 2023 IXPE observations, the IXPE region was ~4 and ~1.8 arcminutes from the center of the instrument FoV, respectively. We note that while the IXPE instrumental half-power diameter (HPD) is 25″, flexure and aspect jitter always somewhat blur the images. While this can be largely removed during typical IXPE observations of bright point sources, in fields with a faint extended emission aspect, correction is more difficult. Despite extra care being taken in aligning the images, such blur remains, and so we adopted generous extraction apertures. This should help to collect most of the photons from the polarized source and make the resulting spectrum less sensitive to the exact positioning of the extraction region. The spectra extracted from the *Chandra* data (corrected for the background extracted from the almost circular region ($\approx 100 \times 94''$) shown with the dashed line in Fig. 2) are shown in Fig. 4. The diffuse X-ray emission of the GC region consists of several spectral components, some of which are highly variable in space and time and contain bright emission lines such as the lines at 6.4 and 6.7 keV of neutral and He-like iron. The former line is due to the reflection of X-rays by the neutral/molecular medium (e.g., Vainshtein & Sunyaev
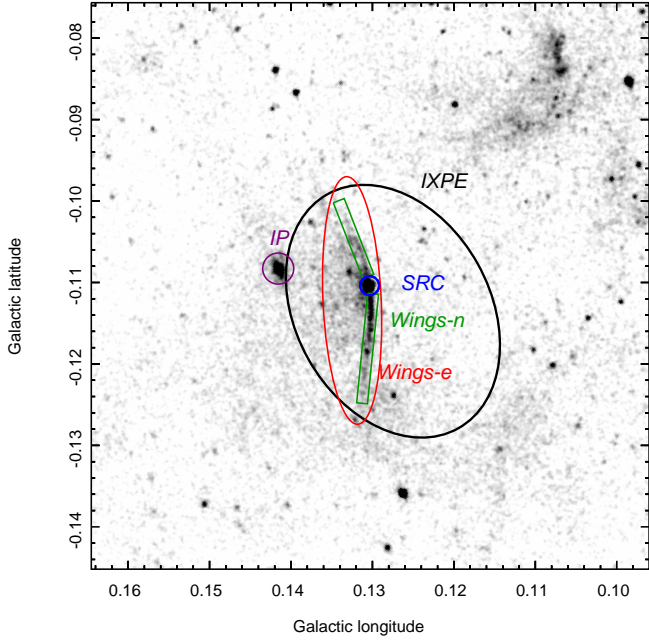
Fig. 3. Regions used for spectral extraction from *Chandra* data. The black ellipse called IXPE is the same as the source region in Fig. 2. The other three regions (SRC, Wings-n, and Wings-e) cover the compact source and the brighter parts of the X-ray bow. The SRC and Wings-n regions do not overlap. Larger regions (Wings-e and IXPE) include all the *Chandra* counts inside them; i.e., the IXPE region includes the counts from SRC, Wings-n, and almost the entire Wings-e counts. The purple circle labeled as IP shows the extraction region for the intermediate polar CXOUGC J174622.7−285218.
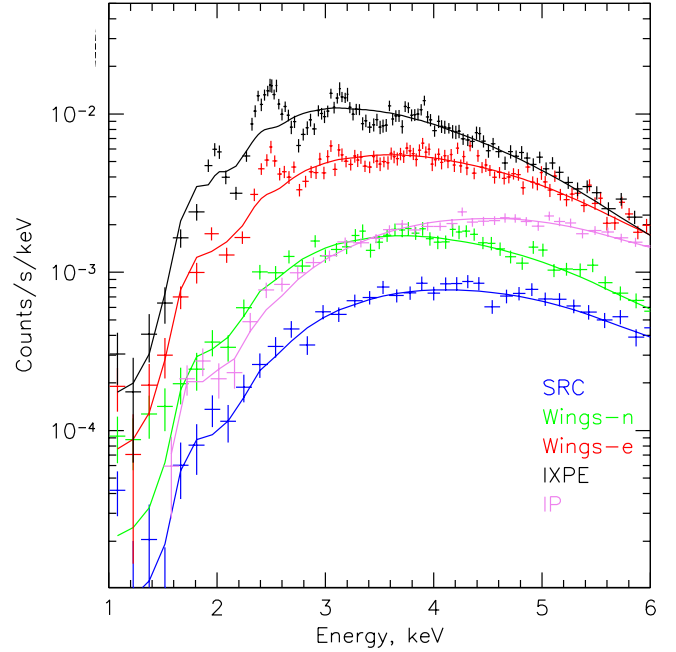

Fig. 4. Background-subtracted *Chandra* spectra in the vicinity of G0.13−0.11. The colors correspond to the regions shown in Fig. 3 and are identified in this figure. The solid lines show the best-fitting absorbed power-law model fits to these spectra. While a pure power law can describe the compact source spectrum (blue) reasonably well, other regions clearly contain a non-negligible contribution of thermal emission that gives rise to emission lines at low energies. The spectrum of the intermediate polar CXOUGC J174622.7−285218 is shown in purple.

1980; Koyama et al. 1996), while the latter is a combination of numerous accreting stellar-mass objects that produce "thermal" spectra (e.g., Revnivtsev et al. 2009). This means that there is no well-defined and "optimal" choice of the background region. Since in this study we are interested in the nonthermal component, the background region was selected to have a comparable mix of the reflection and thermal spectra. No fine-tuning was done when selecting the background region, although we verified that other reasonable choices do not significantly affect our final results. To mitigate the uncertainties associated with the contributions of the reflection component above 6 keV and strong lines below 3 keV coupled with strong low-energy photoelectric absorption, we restricted the analysis of IXPE data to the 3−6 keV band. The higher energy resolution of *Chandra* permits the spectral analysis in a broader band, illustrating strong suppression of X-ray flux below 2−3 keV due to photo-electric absorption with a typical column density $N_{\rm H} \sim 8 \times 10^{22}\,{\rm cm}^{-2}$ (see Table 1).

Simple absorbed power-law model fits to the spectra are shown with solid lines. Clearly, strong emission lines (e.g., of strongly ionized Si or S) are present in the *Chandra* spectrum of the "IXPE" region even after subtracting the spectrum extracted from the background region. Somewhat weaker lines are still seen in the Wings-e spectrum, while the Wings-n and SRC spectra seem to be reasonably well described by the power-law model.

The parameters of the model are given in Table 1. The central bright source, presumably the pulsar itself and possibly a compact part of its PWN, has the hardest spectrum, $\Gamma \sim 1.35$, while the Wings-n and Wings-e regions have significantly softer spectra, $\Gamma \sim 2.2-2.4$. Broadly, these spectral parameters are

consistent with those obtained by Yusef-Zadeh et al. (2002) and Wang et al. (2002), given the difference in the choice of extraction regions and possible variability of the diffuse (reflected) emission. The IXPE region is clearly contaminated by thermal emission below 3−4 keV. However, already at ~5 keV, the fluxes from the Wings-e and IXPE regions are comparable. The Wings-e spectrum itself contains a non-negligible fraction of thermal emission. To set a lower limit on the degree of polarization, we conservatively assumed that the total intensity (i.e., Stokes $I(E)$) of the nonthermal component is described by the Wings-e spectrum (the red lines in Fig. 4). We therefore model the IXPE's $Q(E)$ and $U(E)$ spectra assuming that $I(E)$ is known. With this approach, there are only two free parameters: the degree of polarization, P, and the polarization direction, ϕ. When fitting $Q(E)$ and $U(E)$ spectra, these parameters enter as pre-factors $P\cos 2\phi$ and $P\sin 2\phi$ in front of the *Chandra* $I(E)$ model convolved with the IXPE response to polarized emission. Figure 5 shows the I, Q, and U spectra obtained by IXPE, along with *Chandra*'s Wings-e model convolved with the IXPE response. The IXPE response was averaged over three IXPE modules.

The above assumptions yield the following best-fitting values: PD = 57 ± 18% and angle PA = 21 ± 9°. Setting PD = 0 increases the value of χ^2 by 10.37, which for two degrees of freedom implies a probability ~5.3 × 10^{-3} of a random fluctuation. The corresponding confidence contours are shown in Fig. 6. The high value of the PD is a strong argument in favor of the synchrotron origin of the X-ray emission. The constraints on the polarization angle are shown in Fig. 1. Within uncertainties, the polarization plane is perpendicular to the bright X-ray structure and, also, to the direction of radio filaments co-spatial with the extended X-ray source. This suggests that both the radio and

Table 1. Absorbed power-law model fits to *Chandra* spectra for three regions of G0.11−0.13 (see Fig. 3 for region definition).

Region	$N_{\rm H}$ $(10^{22}\,{\rm cm}^{-2})$	Γ	$F_{2-10\,{\rm keV}}$ $({\rm erg\,s}^{-1}\,{\rm cm}^{-2})$	Area $({\rm arcsec}^2)$	χ^2 (d.o.f.)
"SRC"	7.7 ± 0.6	1.35 ± 0.14	1.1×10^{-13}	54	465 (478)
"Wings-n"	7.6 ± 0.4	2.27 ± 0.12	1.6×10^{-13}	420	506 (478)
"Wings-e"	7.1 ± 0.2	2.40 ± 0.07	5.0×10^{-13}	2213	645 (478)
Entire "IXPE" region	8.1 ± 0.2	3.75 ± 0.07	6.4×10^{-13}	8000	1010 (478)

Notes. The observed $2-10\,{\rm keV}$ fluxes (i.e., including the effects of the low-energy photoelectric absorption) are quoted. The statistical uncertainties in the model parameters $N_{\rm H}$ and Γ are given.
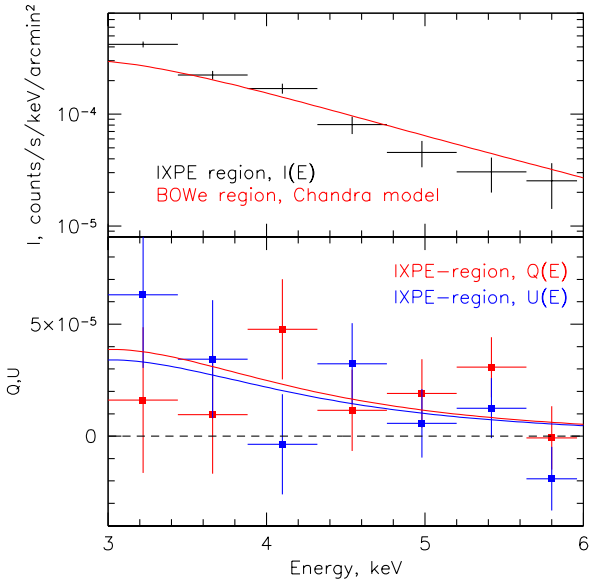

Fig. 5. IXPE spectra. Top panel: IXPE total background-subtracted Stokes $I(E)$ spectrum in the $3-6\,{\rm keV}$ band from the IXPE region (see Figs. 2 and 3) is shown with the black points. The red line in the top panel shows *Chandra*'s Wings-e region model (see Fig. 4) convolved with the IXPE response. Bottom panel: Stokes $Q(E)$ and $U(E)$ spectra of the IXPE region: red and blue points, respectively. The solid lines show the expected spectra for *Chandra*'s Wings-e model and the best-fitting polarization degree PD = $57 \pm 18\%$ and angle PA = $21 \pm 9°$.

X-ray emissions are due to the synchrotron radiation of relativistic electrons in the same magnetic structures.

We note here that when calculating the degree of polarization, we conservatively assumed that essentially all nonthermal flux coming from the IXPE region is polarized (i.e., model Wings-e). If instead only the emission coming from the Wings-n region or from the PWN itself is polarized, then the degree of polarization will only be higher. For instance, substituting the *Chandra*-based Wings-e model with the Wings-n model for $I(E)$ yields PD = $160 \pm 60\%$. A high degree of polarization ($>100\%$) is a plausible outcome of using the incorrect assumption of what fraction of the total signal comes from the polarized source. Apart from the statistical errors already included in the uncertainties of PD estimates, there might be additional uncertainties associated with the limited astrometric quality of IXPE data, although our choice of a large region for spectral extraction will have minimized these uncertainties.

The choice of the background region might affect the shape and normalization of the Wings-e spectral model derived from the *Chandra* spectra. Both the variations in the diffuse emission level and in the absorbing column density can contribute.

Experiments with four different background regions have shown that the predicted flux in the $3-6\,{\rm keV}$ band does not vary by more than 20%. One can therefore consider this as an additional source of systematic uncertainties in the measured PD value, which, however, does not affect the significance of the polarization detection. This background-induced uncertainty is subdominant to the uncertainties associated with the choice of the Wings-e region to extract the reference $I(E)$ spectrum. We also note that the presence of the bright and time-variable intermediate polar (IP) CXOUGC J174622.7−285218 (Muno et al. 2009) in close vicinity of G0.13−0.11 (see Fig. 3) can be considered as a possible source of the polarized signal contamination for IXPE. However, as is evident from Fig. 4, its flux at ~4 keV is similar to that of the Wings-n region. This means that if this IP is the dominant source of polarization, its emission should be almost 100% polarized, which is unlikely. For example, Matt (2004) estimated the maximum degree of polarization in magnetic cataclysmic variables of about 4% produced by the scattering of the thermal radiation.

We reiterate here that spatially resolving contributions of the IP and the diffuse emission can be easily done in the *Chandra* data. However, for IXPE, the coarser angular resolution and the uncertainties with the absolute astrometry (i.e., an apparent shift) complicate the procedure. The photons from IP and the diffuse emission associated with the PWN are mixed in the IXPE images. The choice is therefore between two options: (i) make a smaller and shifted region that excludes IP using *Chandra* images, but might miss a hard–to-quantify fraction of the diffuse/polarized emission or (ii) make a larger region (based on IXPE images) that captures most of the diffuse emission but is contaminated by the IP contribution, which can be removed from the PWN spectrum using *Chandra* data. We decided that the latter option is a more transparent approach, which, however, requires an assumption that the IP emission is not strongly polarized, as supported by the IP polarization models of Matt (2004).

4. Discussion and conclusions

The IXPE data provide two main observational results: (i) the strong polarization of G0.13−11 X-ray emission, PD = $57 \pm 18\%$, and (ii) the polarization direction almost along the Galactic plane. This directly proves that X-ray emission is of synchrotron origin and that the orientation of the magnetic field follows a subsystem of the Radio Arc NTFs[2], which are elongated perpen-

---

[2] The large Faraday rotation measure RM $\sim$ a few $10^3\,{\rm rad\,m}^{-2}$ (e.g., Paré et al. 2019, 2021) complicates the PA determination at radio frequencies and limits reliable polarization measurements to patches of the brightest radio filaments. In contrast, polarization in the X-ray regime does not suffer from Faraday rotation.
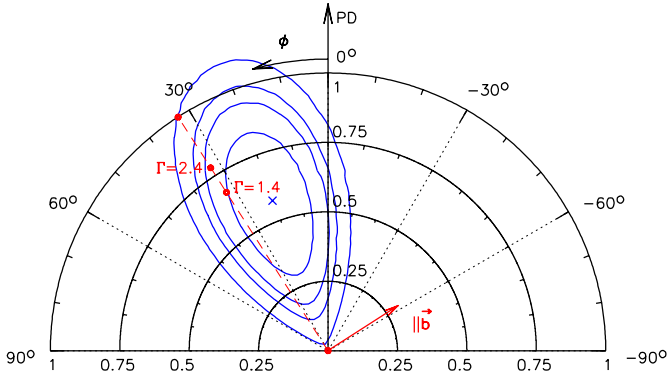
Fig. 6. Confidence regions for polarization degree (PD) and polarization angle (PA; equatorial coordinate system) derived from the IXPE data, assuming that the polarized emission corresponds to the Wings-e spectral model. The blue line shows the contours of the χ^2 statistic after subtraction of the minimum value $\chi^2_{\min}$ reached at PD ≈ 0.57 and PA $\approx 21°$ (marked with a blue cross). The contours show $\Delta\chi^2 = 2.3$, 4.61, 6.17, and 9.21 levels, corresponding to 68.3% (1σ), 90%, 95.4% (2σ), and 99% confidence levels, respectively. The red dashed line illustrates the expected PA in the case, when the electric field vector is parallel to the Galactic plane, and two circles mark the maximum polarization for synchrotron emission for $\Gamma = 1.4$ and 2.4 (as labeled next to them). The outmost contour extends to PD values larger than 1. This is a plausible outcome of our procedure when the $Q(E)$ and $U(E)$ data are taken from IXPE, while $I(E)$ is based on the *Chandra* data extracted from a smaller region, which is supposed to be polarized and might not coincide with true polarized $I(E)$ seen by IXPE.

dicularly to the Galactic plane. These statements are essentially model independent.

These data also prove that the field is well ordered. Indeed, for a perfectly aligned magnetic field and a power-law distribution of relativistic leptons over energy $\propto \gamma^{-p}$ with index p, the degree of the synchrotron emission polarisation is (e.g., Longair 2011)

$$\text{PD}_{\max} = \frac{3p+3}{3p+7} = \frac{3\Gamma}{3\Gamma+2}, \tag{1}$$

where $\Gamma = (p+1)/2$ is the photon index of the observed spectrum (for Γ between 1.4 and 2.2, the maximum degree of polarization is between 68 and 78%). Using the formulation for depolarization of synchrotron emission in a turbulent magnetic field by Bandiera & Petruk (2016), we estimated a ratio of turbulent versus ordered magnetic field energy to be likely smaller than ~1.5. However, the observed PD = $57 \pm 18\%$ is consistent (within uncertainties) even with a perfectly ordered field (see Fig. 6). We note that a high level of polarization can be achieved even in a fully turbulent regime if the turbulence is anisotropic (typically at a level of 2−4), given that polarization is sensitive to the alignment of the magnetic field with a certain direction and is insensitive to field reversals (Bandiera & Petruk 2016). This preferred direction should be maintained across the IXPE spectral extraction region. Indeed, current models of X-ray emission in bright jet-like features associated with PSRs advocate the amplification of the magnetic field via some form of streaming instability, to justify magnetic field values that are typically inferred to be an order of magnitude higher than the surrounding ISM (Bandiera 2008). This might not be needed in the GC environment, where the ambient magnetic field can be high.

The X-ray emission of G0.13−0.11 is co-spatial with a Fermi source 4FGL J1746.4−2852 (Abdollahi et al. 2020)

at GeV energies and a TeV-source HESS J1746−285 (H.E.S.S. Collaboration 2018). The standard leptonic model for broadband radio-TeV objects usually relies on two processes: the synchrotron and inverse Compton (IC) emissions. We defer an in-depth discussion for a forthcoming publication, but we note that the following set of fiducial parameters might explain some of the main characteristics of the G0.13−0.11 broad-band spectrum: $B \sim 100\,\mu\text{G}$ is relevant for the radio–X-ray regime (synchrotron emission) and a combination of the CMB plus local ~eV radiation field with the energy density of the order of $100\,\text{eV cm}^{-3}$ (e.g., Popescu et al. 2017; Niederwanger et al. 2019) is relevant for the photons in the GeV–TeV range produced via IC scatterings. Such a value of the magnetic field strength agrees with the equipartition arguments (e.g., Beck & Krause 2005) based on the measured X-ray flux and the broad-band photon index $\Gamma = 2$, although allowing the index to vary between 1.6 and 2.4 changes B between ~20 and ~800 μG, respectively (see, e.g., Morris 2006, for discussion on various arguments in favor of weaker and stronger fields). The adopted value of $B \sim 100\,\mu\text{G}$ implies that the field energy density is of the same order as the energy density of the radiation and, therefore, the lifetime of leptons emitting at a given frequency is close to the maximum. In this case, X-rays are produced by the leptons with $\gamma \sim 3 \times 10^7$ which have a lifetime consistent with the size of G0.13−0.11, provided that they can propagate with a sizable fraction (~0.2) of the speed of light. For photons with TeV energies, produced by IC scattering of ~eV photons, the cross-section is already subject to the Klein-Nishina suppression, while for the CMB photons, the scattering is still in the Thomson regime, where the cross-section is maximal.

In connection with the fast propagation of relativistic electrons along a filament with a rather strong magnetic field, we note an interesting possible similarity with galaxy clusters, where extended structures in the radio bands are observed both in the cores and outskirts (e.g., Brienza et al. 2021; Rudnick et al. 2022). These structures often have very similar spectral properties (e.g., Rajpurohit et al. 2020). This suggests that relativistic electrons can propagate along the filament with velocities significantly larger than the sound or Alfven speeds in the bulk of the thermal intracluster medium (Churazov et al. 2023). The filaments in both classes of objects might be threads of a strong magnetic field embedded in the medium with a weaker magnetic field. This does not exclude possible amplification of the magnetic field by streaming particles from the PSR.

Apart from the polarized synchrotron X-ray emission of G0.13−0.11, there are many more radio and (fainter) X-ray threads in the same region that are visible in *Chandra* data. Presumably, they are polarized too and, therefore, can contribute to the overall polarization signal from the GC region. It is also possible that even fainter threads are present that are too weak to be detected individually. Since the direction of polarization might be set by the ambient magnetic field, this background polarization signal will also be polarized along the Galactic plane (at least in the areas where "vertical" NTFs are present).

Yet another source of polarized emission is the Compton-scattered emission of the Sgr A* flare(s) that happened hundreds of years ago. This scenario, motivated by the observed hard X-ray continuum and fluorescent lines of neutral iron from dense molecular clouds, was put forward in the 90s (Sunyaev et al. 1993; Markevitch et al. 1993; Koyama et al. 1996). If the continuum emission is scattered light from Sgr A*, it has to be polarized (Churazov et al. 2002) perpendicularly to the direction towards Sgr A*. A weak polarized emission from the

area within a few arcminutes of G0.13−0.11 was indeed detected in the first IXPE observations of the GC region (Marin et al. 2023). The emission from G0.13−0.11 itself was excluded from that analysis to avoid potential contamination. Now we see that there was a good reason to do so. Somewhat ironically, the polarization angles from X-ray threads and reflection are approximately orthogonal to each other and, therefore, can attenuate the net polarization signal if combined. The presence of many faint polarized threads is, therefore, a complication (an interesting one!) for the analysis of IXPE data from the GC. The limited astrometric accuracy of IXPE does not allow for a clean spatial separation of these two components, but a combination of IXPE data with the high spatial resolution of *Chandra*, *XMM-Newton*, and *Chandra* spectra can be used to constrain their contributions. This will be reported elsewhere.

We conclude by saying that IXPE observations show that X-ray emission from G0.13−0.11 is strongly polarized (∼60%) in the direction perpendicular to the bright wings-like X-ray structure and to the nearby radio-emitting filaments, which are part of the GC Radio Arc. While the IXPE angular resolution is not sufficient to spatially resolve polarized emission into individual subarcminute components (i.e., the wings and the fainter diffuse emission to the east of them), the statement of the high degree of polarization is robust. These measurements prove that X-ray emission of filaments associated with BSPWNs has a synchrotron origin, as expected in the baseline scenario of these objects. In particular, X-ray threads of G0.13−0.11 are produced by synchrotron emission of ∼10 TeV leptons gyrating in the ordered magnetic field perpendicular to the Galactic plane. This finding corroborates the scenario that PWNs power not only the X-ray emission but also radio emission of filaments in the GC region (e.g., Wang et al. 2002; Bykov et al. 2017; Barkov & Lyutikov 2019). To this end, a particularly interesting question (to be addressed elsewhere) would be whether the entire Radio Arc is powered by the same mechanism (see Wang et al. 2002 for a relevant discussion).

References

Abdollahi, S., Acero, F., Ackermann, M., et al. 2020, ApJS, 247, 33
Bandiera, R. 2008, A&A, 490, L3
Bandiera, R., & Petruk, O. 2016, MNRAS, 459, 178
Barkov, M. V., & Lyutikov, M. 2019, MNRAS, 489, L28
Barkov, M. V., Lyutikov, M., & Khangulyan, D. 2019, MNRAS, 484, 4760
Beck, R., & Krause, M. 2005, Astron. Nachr., 326, 414
Brienza, M., Shimwell, T. W., de Gasperin, F., et al. 2021, Nat. Astron., 5, 1261
Bykov, A. M., Amato, E., Petrov, A. E., Krassilchtchikov, A. M., & Levenfish, K. P. 2017, Space Sci. Rev., 207, 235
Churazov, E., Sunyaev, R., & Sazonov, S. 2002, MNRAS, 330, 817
Churazov, E., Khabibullin, I., Bykov, A. M., Lyskova, N., & Sunyaev, R. 2023, A&A, 670, A156
de Vries, M., Romani, R. W., Kargaltsev, O., et al. 2022, ApJ, 939, 70
Di Marco, A., Soffitta, P., Costa, E., et al. 2023, AJ, 165, 143
Gaensler, B. M., & Slane, P. O. 2006, ARA&A, 44, 17
Guan, Y., Clark, S. E., Hensley, B. S., et al. 2021, ApJ, 920, 6
H.E.S.S. Collaboration (Abdalla, H., et al.) 2018, A&A, 612, A9
Heywood, I., Camilo, F., Cotton, W. D., et al. 2019, Nature, 573, 235
Heywood, I., Rammala, I., Camilo, F., et al. 2022, ApJ, 925, 165
Kargaltsev, O., Pavlov, G. G., Klingler, N., & Rangelov, B. 2017, J. Plasma Phys., 83, 635830501
Kislat, F., Clark, B., Beilicke, M., & Krawczynski, H. 2015, Astropart. Phys., 68, 45
Koyama, K., Maeda, Y., Sonobe, T., et al. 1996, PASJ, 48, 249
Lang, C. C., Morris, M., & Echevarria, L. 1999, ApJ, 526, 727
LaRosa, T. N., Nord, M. E., Lazio, T. J. W., & Kassim, N. E. 2004, ApJ, 607, 302
Longair, M. S. 2011, High Energy Astrophysics (Cambridge: Cambridge University Press)
Marin, F., Churazov, E., Khabibullin, I., et al. 2023, Nature, 619, 41
Markevitch, M., Sunyaev, R. A., & Pavlinsky, M. 1993, Nature, 364, 40
Matt, G. 2004, A&A, 423, 495
Morris, M. 2006, J. Phys. Conf. Ser., 54, 1
Muno, M. P., Bauer, F. E., Baganoff, F. K., et al. 2009, ApJS, 181, 110
Niederwanger, F., Reimer, O., Kissmann, R., et al. 2019, Astropart. Phys., 107, 1
Olmi, B., & Bucciantini, N. 2019, MNRAS, 490, 3608
Olmi, B., & Bucciantini, N. 2023, PASA, 40, e007
Paré, D. M., Lang, C. C., Morris, M. R., Moore, H., & Mao, S. A. 2019, ApJ, 884, 170
Paré, D. M., Purcell, C. R., Lang, C. C., Morris, M. R., & Green, J. A. 2021, ApJ, 923, 82
Pavan, L., Bozzo, E., Pühlhofer, G., et al. 2011, A&A, 533, A74
Popescu, C. C., Yang, R., Tuffs, R. J., et al. 2017, MNRAS, 470, 2539
Rajpurohit, K., Hoeft, M., Vazza, F., et al. 2020, A&A, 636, A30
Revnivtsev, M., Sazonov, S., Churazov, E., et al. 2009, Nature, 458, 1142
Rudnick, L., Brüggen, M., Brunetti, G., et al. 2022, ApJ, 935, 168
Sunyaev, R. A., Markevitch, M., & Pavlinsky, M. 1993, ApJ, 407, 606
Tsuboi, M., Inoue, M., Handa, T., et al. 1986, AJ, 92, 818
Vainshtein, L. A., & Sunyaev, R. A. 1980, Sov. Astron. Lett., 6, 353
Vikhlinin, A., Burenin, R. A., Ebeling, H., et al. 2009, ApJ, 692, 1033
Wang, Q. D., Lu, F., & Lang, C. C. 2002, ApJ, 581, 1148
Weisskopf, M. C., Soffitta, P., Baldini, L., et al. 2022, J. Astron. Telesc. Instrum. Syst., 8, 026002
Yusef-Zadeh, F., Morris, M., & Chance, D. 1984, Nature, 310, 557
Yusef-Zadeh, F., Law, C., & Wardle, M. 2002, ApJ, 568, L121
Yusef-Zadeh, F., Hewitt, J. W., & Cotton, W. 2004, ApJS, 155, 421
Zhang, S., Zhu, Z., Li, H., et al. 2020, ApJ, 893, 3

[1] Max Planck Institute for Astrophysics, Karl-Schwarzschild-Str. 1, 85741 Garching, Germany
e-mail: churazov@mpa-garching.mpg.de
[2] Space Research Institute (IKI), Profsoyuznaya 84/32, Moscow 117997, Russia
[3] Universitäts-Sternwarte, Fakultät für Physik, Ludwig-Maximilians-Universität München, Scheinerstr. 1, 81679 München, Germany
[4] Université de Strasbourg, CNRS, Observatoire Astronomique de Strasbourg, UMR 7550, 67000 Strasbourg, France
[5] INAF Osservatorio Astrofisico di Arcetri, Largo Enrico Fermi 5, 50125 Firenze, Italy
[6] Dipartimento di Fisica e Astronomia, Università degli Studi di Firenze, Via Sansone 1, 50019 Sesto Fiorentino, FI, Italy
[7] Istituto Nazionale di Fisica Nucleare, Sezione di Firenze, Via Sansone 1, 50019 Sesto Fiorentino, FI, Italy
[8] INAF Istituto di Astrofisica e Planetologia Spaziali, Via del Fosso del Cavaliere 100, 00133 Roma, Italy
[9] Agenzia Spaziale Italiana, Via del Politecnico snc, 00133 Roma, Italy

[10] Center for Astrophysics, Harvard & Smithsonian, 60 Garden St, Cambridge, MA 02138, USA

[11] NASA Marshall Space Flight Center, Huntsville, AL 35812, USA

[12] Dipartimento di Fisica, Università degli Studi di Roma "La Sapienza", Piazzale Aldo Moro 5, 00185 Roma, Italy

[13] Istituto Nazionale di Fisica Nucleare, Sezione di Roma "Tor Vergata", Via della Ricerca Scientifica 1, 00133 Roma, Italy

[14] Dipartimento di Matematica e Fisica, Università degli Studi Roma Tre, Via della Vasca Navale 84, 00146 Roma, Italy

[15] Department of Physics and Astronomy, Louisiana State University, Baton Rouge, LA 70803, USA

[16] Department of Physics and Kavli Institute for Particle Astrophysics and Cosmology, Stanford University, Stanford, CA 94305, USA

[17] Istituto Nazionale di Fisica Nucleare, Sezione di Pisa, Largo B. Pontecorvo 3, 56127 Pisa, Italy

[18] Astronomical Institute of the Czech Academy of Sciences, Boční II 1401/1, 14100 Praha 4, Czech Republic

[19] Guangxi Key Laboratory for Relativistic Astrophysics, School of Physical Science and Technology, Guangxi University, Nanning 530004, PR China

[20] Instituto de Astrofísica de Andalucía – CSIC, Glorieta de la Astronomía s/n, 18008 Granada, Spain

[21] INAF Osservatorio Astronomico di Roma, Via Frascati 33, 00040 Monte Porzio Catone, RM, Italy

[22] Space Science Data Center, Agenzia Spaziale Italiana, Via del Politecnico snc, 00133 Roma, Italy

[23] INAF Osservatorio Astronomico di Cagliari, Via della Scienza 5, 09047 Selargius, CA, Italy

[24] Dipartimento di Fisica, Università di Pisa, Largo B. Pontecorvo 3, 56127 Pisa, Italy

[25] Istituto Nazionale di Fisica Nucleare, Sezione di Torino, Via Pietro Giuria 1, 10125 Torino, Italy

[26] Dipartimento di Fisica, Università degli Studi di Torino, Via Pietro Giuria 1, 10125 Torino, Italy

[27] Science and Technology Institute, Universities Space Research Association, Huntsville, AL 35805, USA

[28] Institut für Astronomie und Astrophysik, Universität Tübingen, Sand 1, 72076 Tübingen, Germany

[29] RIKEN Cluster for Pioneering Research, 2-1 Hirosawa, Wako, Saitama 351-0198, Japan

[30] X-ray Astrophysics Laboratory, NASA Goddard Space Flight Center, Greenbelt, MD 20771, USA

[31] Yamagata University, 1-4-12 Kojirakawa-machi, Yamagata-shi 990-8560, Japan

[32] Osaka University, 1-1 Yamadaoka, Suita, Osaka 565-0871, Japan

[33] University of British Columbia, Vancouver, BC V6T 1Z4, Canada

[34] International Center for Hadron Astrophysics, Chiba University, Chiba 263-8522, Japan

[35] Institute for Astrophysical Research, Boston University, 725 Commonwealth Avenue, Boston, MA 02215, USA

[36] Department of Astrophysics, St. Petersburg State University, Universitetsky Pr. 28, Petrodvoretz, 198504 St. Petersburg, Russia

[37] Department of Physics and Astronomy and Space Science Center, University of New Hampshire, Durham, NH 03824, USA

[38] Physics Department and McDonnell Center for the Space Sciences, Washington University in St. Louis, St. Louis, MO 63130, USA

[39] Istituto Nazionale di Fisica Nucleare, Sezione di Napoli, Strada Comunale Cinthia, 80126 Napoli, Italy

[40] MIT Kavli Institute for Astrophysics and Space Research, Massachusetts Institute of Technology, 77 Massachusetts Avenue, Cambridge, MA 02139, USA

[41] Graduate School of Science, Division of Particle and Astrophysical Science, Nagoya University, Furo-cho, Chikusa-ku, Nagoya, Aichi 464-8602, Japan

[42] Hiroshima Astrophysical Science Center, Hiroshima University, 1-3-1 Kagamiyama, Higashi-Hiroshima, Hiroshima 739-8526, Japan

[43] Department of Physics, University of Hong Kong, Pokfulam, Hong Kong

[44] Department of Astronomy and Astrophysics, Pennsylvania State University, University Park, PA 16801, USA

[45] Université Grenoble Alpes, CNRS, IPAG, 38000 Grenoble, France

[46] Department of Physics and Astronomy, University of Turku, 20014 Turku, Finland

[47] INAF Osservatorio Astronomico di Brera, Via E. Bianchi 46, 23807 Merate, LC, Italy

[48] Dipartimento di Fisica e Astronomia, Università degli Studi di Padova, Via Marzolo 8, 35131 Padova, Italy

[49] Dipartimento di Fisica, Università degli Studi di Roma "Tor Vergata", Via della Ricerca Scientifica 1, 00133 Roma, Italy

[50] Department of Astronomy, University of Maryland, College Park, MA 20742, USA

[51] Mullard Space Science Laboratory, University College London, Holmbury St Mary, Dorking, Surrey RH5 6NT, UK

[52] Anton Pannekoek Institute for Astronomy & GRAPPA, University of Amsterdam, Science Park 904, 1098 XH Amsterdam, The Netherlands

[53] Dipartimento di Fisica, Università degli Studi di Roma "Tor Vergata", Via della Ricerca Scientifica 1, 00133 Roma, Italy